Mechanical properties of 3D printed CMT-WAAM 316 LSi stainless steel walls

Andrade, D. G.; Tankova, T.; Zhu, C.; Branco, R.; da Silva, L. Simões; Rodrigues, D. M.

DOI
10.1016/j.jcsr.2024.108527

Publication date
2024

Document Version
Final published version

Published in
Journal of Constructional Steel Research

Journal of Constructional Steel Research 215 (2024) 108527

Contents lists available at ScienceDirect

Journal of Constructional Steel Research

journal homepage: www.elsevier.com/locate/jcsr

Mechanical properties of 3D printed CMT-WAAM 316 LSi stainless steel walls

D.G. Andrade [a,*], T. Tankova [a,b], C. Zhu [c], R. Branco [c], L. Simões da Silva [a], D.M. Rodrigues [d]

[a] University of Coimbra, ISISE, ARISE, Department of Civil Engineering, Coimbra, Portugal
[b] Delft University of Technology, Department of Engineering Structures, the Netherlands
[c] University of Coimbra, CEMMPRE, ARISE, Department of Mechanical Engineering, Portugal
[d] University of Coimbra, ISISE, ARISE, Department of Mechanical Engineering, Coimbra, Portugal

ARTICLE INFO

Keywords:
Stainless steel
Directed energy deposition
Wire arc additive manufacturing
Mechanical properties
Thermal analysis

ABSTRACT

The use of 3D printed stainless steel requires a deep knowledge of its mechanical properties. This paper presents material characterisation of 316LSi austenitic stainless-steel coupons manufactured by CMT-WAAM, considering different deposition directions. The specimens were tested according to ISO 6892-1, the fractures surfaces were examined by SEM for machined and as-built conditions. The material was subject to hardness test and deep microstructural analyses, to assess the anisotropy in material properties at the micro and macro scales, respectively. A thermal analysis performed by infrared thermography of the material deposition in CMT-WAAM was also performed to establish the influence of the temperature evolution (versus time and position) on the microstructural and mechanical properties of the deposited walls. Finally, a statistical assessment was carried out, including results available in the literature and a material model available in the literature was adjusted to the test results, enabling to conclude that it is possible of accurately reproducing the uniaxial stress-strain behaviour, therefore providing a necessary input for the design of steel structures with 3D printed stainless steel.

1. Introduction

Nowadays, additive manufacturing (AM) is rapidly growing due to the possibility to execute different shapes as an alternative to casting and/or machining that require intermediate steps associated with generation of waste. AM is an effective solution for numerous engineering applications since it can be performed in all types of near-net shapes and dimensions. In AM, metallic materials may be produced by direct energy deposition (DED) processes, which may use electric arcs, lasers, or electron beams as heat sources to fuse the feedstock material into the final shape. Although the processes that use laser or electron beams can be employed to produce components with very high accuracy, wire arc additive manufacturing (WAAM) techniques show other benefits, namely it is an economic process with high deposition rates, being suitable for the construction and/or repair of large-scale metallic components with complex geometries [1–3].

WAAM is usually referred to as being a near-net-shape technique due to its relatively poor surface finish. Many WAAM parts may be utilized in their as-built condition, such as the pedestrian MX3D bridge [4] and excavator arm [5], or undergo post-machining processing operations using hybrid equipment which integrates additive and subtractive manufacturing technologies [6]. Studying both as-built and machined samples is crucial, as it provides valuable insights into the material properties and structural integrity, enabling a comprehensive understanding of the process and facilitating decision-making for optimizing the manufacturing and post-processing strategies.

Among metals, stainless steel (SS) production has the highest growth rate percentage increase per year due to its corrosion resistance and mechanical properties, at room and high temperatures [7], where the austenitic stainless steels (ASS), for example, are usually used in aeronautical, marine, nuclear, and chemical industries [8,9]. However, owing to the novelty of the DED processes, their application in the production of ASS parts still requires the characterisation of the material deposition conditions and the analysis of its influence on the microstructural and mechanical properties of the deposited material, to enable their use in engineering applications, guarantying quality assurance and design.

Table 1 summarises a few of the most recent works on tensile and microstructural properties of 316L SS components produced by WAAM, where Gas Tungsten Arc Welding (GTAW), Gas Metal Arc Welding

* Corresponding author.
E-mail address: david.andrade@uc.pt (D.G. Andrade).

https://doi.org/10.1016/j.jcsr.2024.108527
Received 22 June 2023; Received in revised form 17 January 2024; Accepted 4 February 2024
Available online 13 February 2024

(GMAW), and Cold Metal Transfer (CMT) were the main techniques used to produce 316L WAAM components.

Most of these studies reported defected-free parts. The microstructure analyses showed that the deposited material mainly consists of layer band austenitic dendrites vertically oriented, with some ferrite and sigma phases [8–16]. Nonetheless, according to Wang et al. 2019 [12], the arc mode may lead to different grain morphologies, i.e. using the SpeedArc WAAM mode led to a finer solidification structure due to the lower heat accumulation and faster thermal cycles. Long et al. 2022 [8] also promoted grain refinement and reduced the precipitation of brittle phases by using a coolant system. On the other hand, Lee 2020 [11] observed that during the fabrication of a 316L wall, the cooling rates decreased with the layer height, which increased the secondary dendrite arm spacing size.

Due to the operational conditions of the WAAM process, the repeated thermal cycles make the prediction of mechanical properties quite challenging. Several works analysed the tensile strength of WAAM parts and reported that the samples exhibited ductile fracture mode and that the tensile properties exceeded the industry requirements for 316L SS [9,19,22]. Moore et al. 2019 [23] also reported that it is possible to obtain 316L WAAM components with very high fracture toughness. However, most of these works only tested machined coupons, neglecting the influence of the surface finishing on the mechanical properties of the AM parts. Despite this, due to the preferential orientation of the solidified grains, it was found that most of the produced components exhibited anisotropic mechanical properties [13,16,18,19]. For instance, lower strength values in the vertical orientation were registered by Wang et al. 2020 [13] and Rodriguez et al. 2018 [18], while higher strength values in the vertical orientation were registered by Xie et al. 2020 [16] and Wu et al. 2019 [19].

The WAAM heat input is an important factor in determining the component microstructure and morphology, and in this way the mechanical strength of the components. Yang et al. 2017 [24] investigated the thermal evolution during the deposition of a thin-wall part in H08Mn2Si steel produced by GMAW-WAAM with an infrared camera and observed that there is a heat accumulation with the increase of the printing time. The authors also observed that increasing the cooling time between layers led to a decrease in the mean temperature, leading to faster thermal cycles, allowing the production of parts with better surface finish. However, the knowledge on the temperature distribution and evolution with time during the production of WAAM components is still scarce, due to the very narrow range of deposition conditions tested.

Despite the advancements in WAAM, uncertainties remain concerning the process thermal cycles and their relationship with the material structural performance, degree of anisotropy and sensitivity to as-built geometry. To address these issues, in this paper, a deep analysis of the WAAM thermal cycles and of the temperature distribution, along the building and printing directions, during the production of 316LSi SS thick walls, was performed using thermography. A microstructural characterisation was also performed, and the results were related with the thermal data. The mechanical strength of the produced components was assessed by testing machined and as-built coupons, obtained from the printed wall in different orientations (0°, 45°, 90°) relative to the printing direction. Hardness measurements were also performed to assess any mismatching in mechanical properties between the different layers and microstructural features. Finally, the mechanical tests were compared with the results available in the literature and adjusted to available material models.

2. Experimental procedure

2.1. Manufacturing of the WAAM parts

Two wall plates with dimensions of 300 × 300 × 9 mm were fabricated using a CMT Fronius TPS 400i welding machine, guided by an ABB IRB 4600 robot. Fig. 1 shows the appearance of the fabricated walls. The feedstock material used was an SS 316LSi wire with 1.0 mm diameter. Table 2 and Table 3 summarise the chemical composition of the feedstock material, as provided by the manufacturer, and the minimum expected tensile properties for the deposited metal, as defined by the EN ISO 14343 standard [25], respectively. The fabrication process was performed using optimised operational conditions, i.e. travel speed of 10 mm/s, wire feed rate of 7.5 m/min, arc voltage of 13 V, arc current of 120 A, heat input of 0.125 kJ/mm [17], deposition rate of 2.9 kg/h, and M12 shielding gas (98% Ar + 2% CO_2) with a flow rate of 10 L/min. The heat input in the current work was inferior to that used by the other authors in WAAM, even those using the CMT technology (see Table 1). The wall printing was conducted in a 20 mm thick substrate of the same grade as the material being deposited and properly clamped to the working table to prevent any distortion during manufacturing.

The scanning paths are schematised in Fig. 2, which shows that three passes were performed sequentially to produce each layer. First, the edge passes were produced in the same direction and then, an infill run was performed, in the opposite direction. The positioning between two

Table 1
Works that have characterised the microstructural evolution and the mechanical properties of 316L SS components manufactured by WAAM.

Author	WAAM process	Wire diameter [mm]	Current [I]	Voltage [V]	Wire feed rate [m/min]	Scan rate [mm/min]	Heat input [17] [kJ/mm]	Deposition rate [kg/h]	Internal Defects
Chen et al. 2017 [9]	GMAW	1.2	300	28	10	600	0.67	5.4	no
Rodriguez et al. 2018 [18]	CMT	1	150–220	14.2–26.2	8–10	600–1000	0.17–0.35	3–3.7	no
Rodriguez et al. 2018 [18]	GTAW	1	220–268	15.5	4.2–5	700–800	0.18–0.19	1.1–1.9	no
Wang et al. 2019 [12]	Speed Pulse/ Speed Arc	1.2	140–135	19.5–22.1	4.5	600	0.22–0.24	2.4	no
Wu et al. 2019 [19]	GMAW	0.8	60–100	15.7–18.8	3.8–7	250–350	0.15–0.3	0.9–1.7	no
Wang et al. 2020 [13]	CMT	1	150	14.1	11	700	0.15	4.1	voids
Xie et al. 2020 [16]	CMT + P	1.2	140	18.8	7.4	600	0.21	4.0	no
Chen et al. 2021 [20]	CMT	1.2	144	19	5	360	0.36	2.7	no
Kannan et al. 2021 [15]	GMAW	1.2	160	16.4	5.2	250	0.50	2.4	no
Park and Lee 2021 [10]	CMT	1.2	120	11.2	3.6	500	0.13	2.0	no
Belotti et al. 2022 [21]	GMAW	1	160	20.5	8.5	750	0.21	3.2	voids

Fig. 1. Macroscopic view of the fabricated wall.

consecutive passes was 2.5 mm. Furthermore, a layer increment of 3.5 mm was used. The deposition direction in two adjacent layers was interchanged. Dwelling times of 15 s, between passes, was used. This strategy was used to achieve a more uniform temperature distribution across the wall cross-section, to minimise thermal gradients, to reduce residual stresses, and to obtain better dimensional control of the wall.

During the WAAM process, the thermal cycles experienced by the material during deposition were measured using a FLIR A655sc thermographic camera, where the infrared temperature measurement requires the definition of the material surface emissivity. For the temperature acquisition, an emissivity value of 0.5 was used, throughout the entire process, which was calculated from the literature, considering the values used by other authors [24,26–30].

2.2. Characterisation of the WAAM parts

After the deposition, quasi-static tensile tests at room temperature were performed, according to ISO 6892 [31], in a W + B LFV 600kN machine, using an axial extensometer. As shown in Fig. 3, tensile coupons were machined from the produced walls in horizontal, inclined and vertical orientations, with a relative angle of 0°, 45° and 90° between the print layer direction and the principal axis of the tensile specimen, respectively. For each of the horizontal, inclined and vertical orientations, a total of 6 coupons were tested. In half of the tensile specimens, the top and bottom surfaces were milled to eliminate the influence of the surface finish on the mechanical properties, while the other half was tested in the as-built condition. The tensile specimen geometry for the as-built and machined conditions is represented in Fig. 3b and c, respectively. The cross-sectional area for the as-built samples was determined with a calliper by measuring thirty points along the gauge length of the coupon, with each measurement point spaced 1 mm apart. The measured values were then used to determine the average cross-sectional area of the specimen. After the monotonic tensile tests, the fracture surface characteristics of the tested samples were examined by means of a Carl-Zeiss Gemini 500 FE-SEM scanning electron microscope.

To complement the information from the stress-strain curves, microhardness measurements were performed using a Shimadzu Microhardness Tester, with 200 g load and 15 s holding time. The microhardness analysis was carried out in various regions along the wall, more precisely, along the normal (ND), longitudinal (LD) and transverse (TD) directions, relative to the layer's orientation (Fig. 3).

The microstructural analysis was performed using an optical microscope (Leica DM 4000 M LED). Metallographic samples were extracted along all printing directions, grounded, polished and etched with Aqua Regia (30 ml H_2O, 20 ml HCl, 15 ml HNO_3) [32].

3. Results and discussion

3.1. Thermal analysis

The maximum temperatures recorded for the external passes, during the deposition of the first 28 layers, are shown in Fig. 4a, where no results are shown for the second pass because the camera viewing angle became obstructed after the first pass, compromising the temperature acquisition. Fig. 4b and c represent the evolution of the temperature, along the printing direction, for the first pass of the layers number 10 and 20, and Fig. 4d shows the evolution with time of the maximum temperatures recorded for the first 28 layers. The data in Fig. 4b and c show that independently of the layer, lower temperatures were registered at the beginning of each new pass, and that a peak temperature was registered before steady state temperatures were reached. These low temperatures registered at the beginning of the acquisition, which are below the melting point of the alloy, indicate error in the temperature acquisition, at the start of each new set of measurements. This error may be attributed to the interference of the arc with the optical acquisition system, at the beginning of each layer, being the reason why the temperature peak was always registered after a constant value of torch

Table 3
Expected minimum tensile properties of the deposited metal (316LSi) [25].

	Yield Stress [MPa]	Ultimate tensile strength [MPa]	Elongation [%]
316LSi	320	510	25

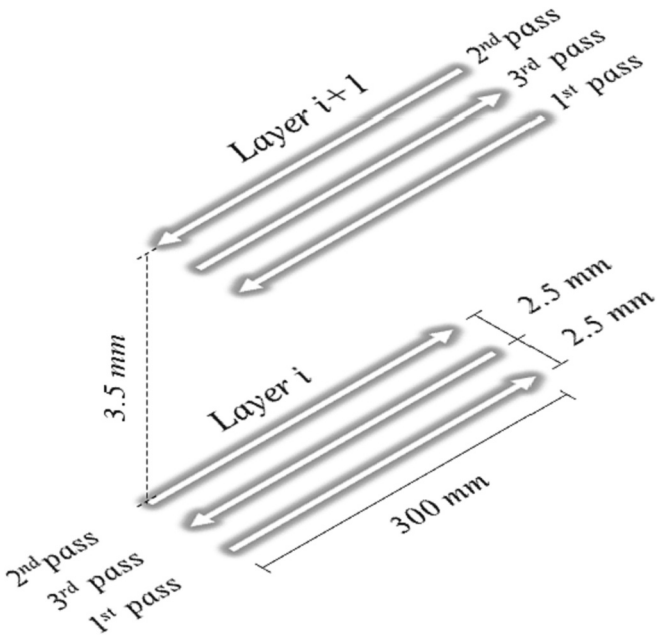

Fig. 2. Schematic representation of the tool path.

Table 2
Chemical composition of the 316LSi feedstock wire (wt%).

Feedstock wire	C	Si	Mn	P	S	Cr	Ni	Mo	Cu	Fe
316LSi	0.017	0.810	1.710	0.026	0.006	18.370	11.270	2.560	0.070	Bal.

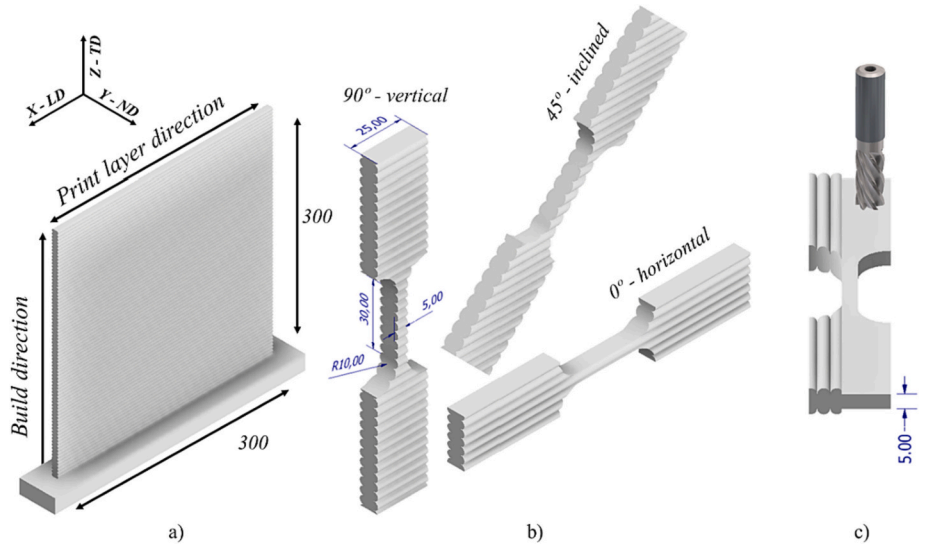

Fig. 3. Schematic representation of the geometry and orientations of the (a) printed wall, (b) as-built tensile coupons and (c) machined tensile coupons.

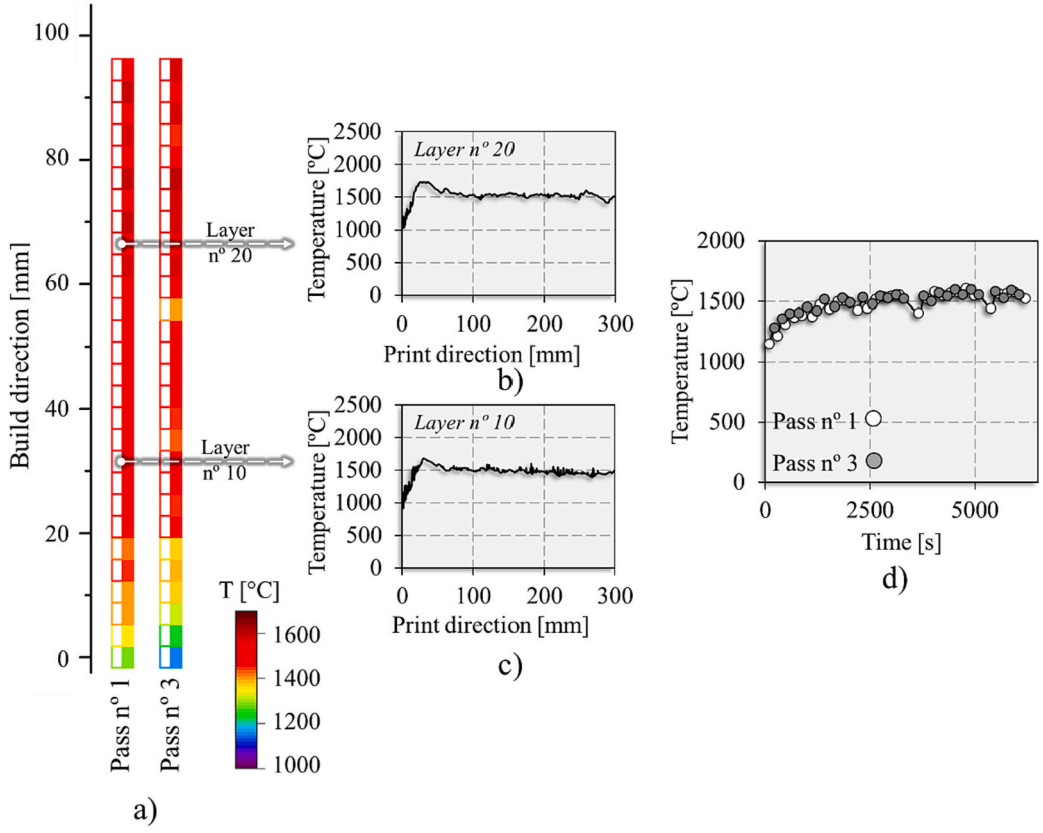

Fig. 4. (a) Evolution of the average maximum temperature for different printing layers/passes, (b and c) maximum temperature evolution, along the printing direction, for the first pass of layers 10 and 20, (d) maximum temperature evolution with the printing time.

displacement (Fig. 4b and c). Due to this problem, the maximum temperatures in Fig. 4a and d, correspond to the average of the temperatures registered during the steady state period in Fig. 4b and c.

The set of images in Fig. 4 clearly shows that, despite the wall was constructed by the successive deposition of multi-pass layers, the thermal history became steady state after 6 layers were deposited. This steady state maximum temperature, of around 1500 °C, was kept constant, during the layer's deposition, for almost the entire wall manufacturing process. The only exception was the period corresponding to the deposition of the first 6 layers, for which the thermal conduction to the substrate had an important role in the heat dissipation, inducing fast cooling of the deposited material.

Fig. 5 shows the evolution of the temperature with time (thermal cycles), in different locations of the wall, as schematised by the measurement sites, 1 to 7, in Fig. 5a. The thermal cycles along the building (locations 1 to 5) and printing (locations 1, 6 and 7) directions are plotted in Fig. 5b to 5e. In Fig. 5b, which represents the thermal history along the building direction, the thermal cycles are represented

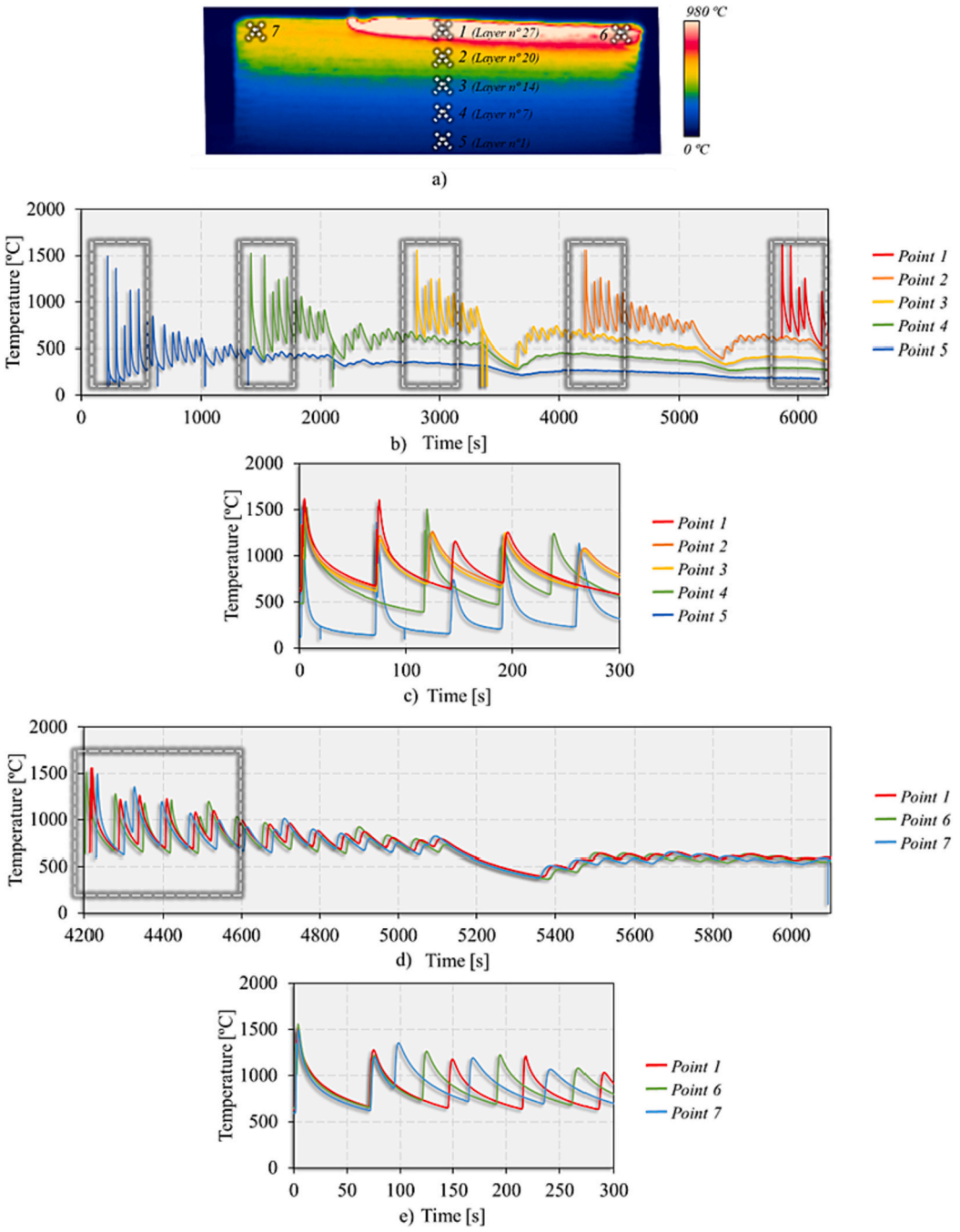

Fig. 5. Wall thermal cycles: (a) schematic representation of the measurement sites, (b and c) evolution of the thermal cycles along the building direction and (d and e) evolution of the thermal cycles along the printing direction.

sequentially, in the time scale, respecting the time interval between successive layers. In Fig. 5c, the portion of the thermal cycles signalised by rectangles in Fig. 5b, are represented in a graphic in which the time scales relative to the different thermal cycles were adjusted for enabling the direct comparison of the results, by enhancing the differences of the heating and cooling rates at the different locations. As Fig. 4, Fig. 5b and c also enable to conclude that steady state heat transfer is reached after the deposition of the first passes. In fact, analysing the thermal evolution at location 5, in the first deposited layers, close to the substrate, it is possible to conclude that the temperatures were lower, and the cooling rates faster, than that registered for the other locations, which may be attributed to the substrate heatsink effect. In addition, for location 4, which was the second closest to the substrate, even though the peak temperatures were similar to those at locations 1 to 3, the cooling rates were also faster, due to the heat dissipation through the substrate. Contrary to this, the thermal cycles in locations 1 to 3 display heating and cooling rates very similar, indicating the attainment of steady state heat transfer. The only noticeable differences between the thermal cycles observed in Fig. 5b, for locations 1 to 3, are related to the torch movement strategy (Fig. 2). Another important conclusion is that, while, in locations 1 to 3, the peak temperature registered during the deposition of the successive layers decreased with time, the minimum temperature remained constant, which shows that the dwelling time between layers was enough to ensure a constant interlayer temperature, which according to the figure was equal to around 700 °C.

Fig. 5d and e, where the thermal cycles at different locations along

the printing direction are compared, corroborate all the assumptions made when analysing the previous figures. However, in addition, Fig. 5d and e also show that the thermal history is also very similar along the printing direction. As reported before, the torch movement strategy was the main factor affecting the thermal history.

The evolution of the maximum temperature in a certain instant of time, with the distance, in the building and in the printing directions (Fig. 6a and b), are displayed in Fig. 6c to 6e. As it is also schematised in the figure, the temperature distributions were analysed in two instants, one when the torch was in the middle of the wall (Fig. 6a), and the other, when the torch was in the edge of the wall, where the layer deposition finishes (Fig. 6b). The maximum temperature distributions in the printing and building directions, plotted in Fig. 6c to 6e, correspond to the deposition of the 5th, 20th and 28th layers, i.e. before (5th layer) and after (20th and 28th layers) steady-state conditions were reached. Analysing Fig. 6c and d, in which the maximum temperature distributions along the printing direction, when the torch was in the middle and in the edge of the wall, respectively, are plotted, it is possible to conclude, in first, that the thermal gradients were steeper in front, than behind the molten pool, where the solidification and phase transformations take place, and in second, that the maximum temperatures had very similar values in layers 20 and 28, which, again, corroborates the thermal stabilisation assumption.

The maximum temperature distributions in the building direction for an instant when the torch was in the middle of the wall, are plotted in Fig. 6e. Comparing the data in this figure, with that in Fig. 6c and d, it is possible to conclude that the temperature gradients were much steeper in the building than in the printing direction, which indicates that the heat of the molten pool is mainly dissipated downward, in the vertical direction, being responsible for the similarities in thermal cycles in locations 1 to 3, in Fig. 5. The steady state thermal cycles had important influence on the microstructure evolution upon cooling, and in this way, on deposited material properties, as it will be shown in the next.

3.2. Morphological and microstructural characterisation

The parts produced by WAAM are usually referred to as near-net shape, due to their rough surface finish. The morphology and surface quality of the walls produced in this research is shown in Fig. 7, where the surface finishing can be analysed. Fig. 7a outlines the as-built wall, representing the local thickness evolution along the height of the sample, and Fig. 7b shows the histogram of the wall thickness, calculated from the colour maps in Fig. 7a. The data shows that the produced wall presented some periodically corrugated morphology between the successive layers. According to the histogram, the average wall thickness was 8.7 mm, ranging from a maximum of 9.4 mm to a minimum of 7.4 mm.

Fig. 7c shows an image of a machined sample featuring a uniform cross-section. This sample was obtained by machining the as-built specimen, wherein an average thickness of 3.7 mm was removed from its original cross-section. In the figure, the deposited layers are visible, with average height of each layer varying between 3.53 and 3.75 mm. Furthermore, the analysis of the samples shows fully dense samples with no other defects such as cracks, pores or improper fusion zones that may lead to delamination. The absence of defects shows the suitability of the operational strategy used to produce high-quality SS products by CMT-WAAM.

The microstructural evolution among the deposited layers is shown in Fig. 8, where the locations from which the micrographs in Fig. 8e to 8j were taken, are marked in Fig. 8a and are shown in Fig. 8b to 8d. The macrograph in Fig. 8b represents the ND-TD plane of the sample and it shows that the layers display a semi-elliptical morphology all along the thickness cross-section. In the same way, the macrographs of the LD-TD (Fig. 8c) and LD-ND (Fig. 8d) planes, also show that the fusion lines were parallel to each other, due to the layer-by-layer deposition strategy.

Fig. 8e to 8h, which show the evolution of the microstructures inside the semi-elliptical morphology of the individual layers, from its top to its bottom, enable to observe columnar grains which grow perpendicularly to the fusion lines (Fig. 8g and h). However, moving upward, vertically, inside the layer, it is also possible to observe a more equiaxed structure (Fig. 8f), which, according to references [10, 33], results from the low temperature gradient inside of the molten pool. This assumption is corroborated by the temperature measurements performed in the current work, which shows that the layers close to the last to be deposited remain at very high temperatures (around 700 °C), during a longer period. Shortly after the next layer is printed, a portion of this equiaxed structure, remelts, leading once again to the formation of columnar grains in the next layer (Fig. 8e, i and j), followed again by equiaxed structures. This process is repeated throughout the manufacturing process, forming periodic microstructural bands along the building

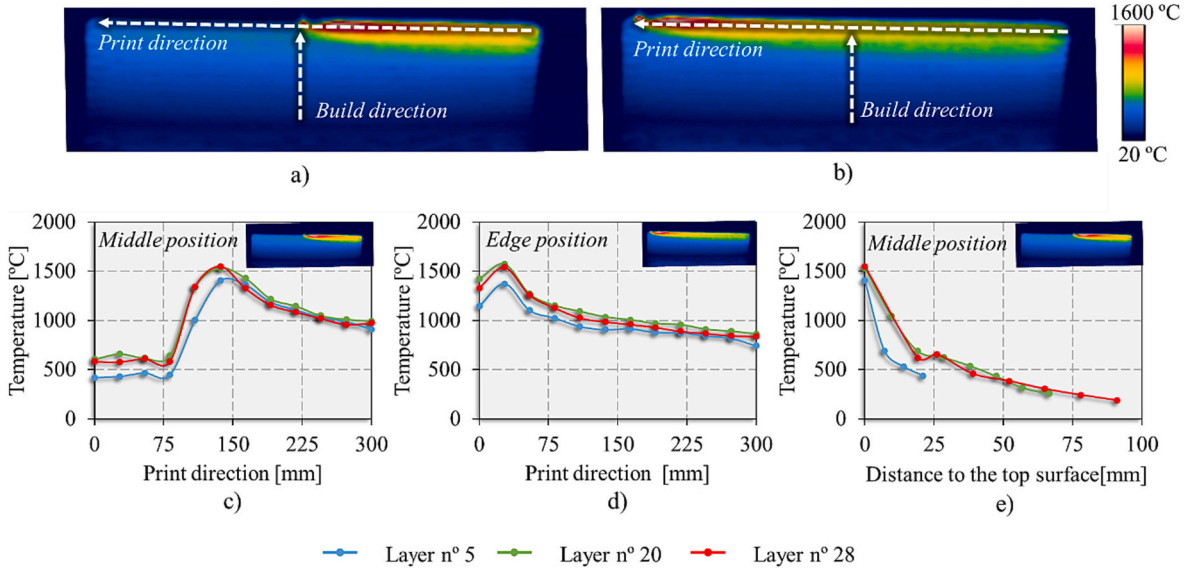

Fig. 6. Schematic representation of the temperature measurement sites along the building and printing directions, during the printing of layers 5th, 20th and 28th, for when the torch was in the (a) middle and (b) edge position of the wall. Temperature distribution along the printing direction for when the torch was in the (c) middle and (d) edge positions. Temperature distribution along the building direction (e) for when the torch was in the middle position.

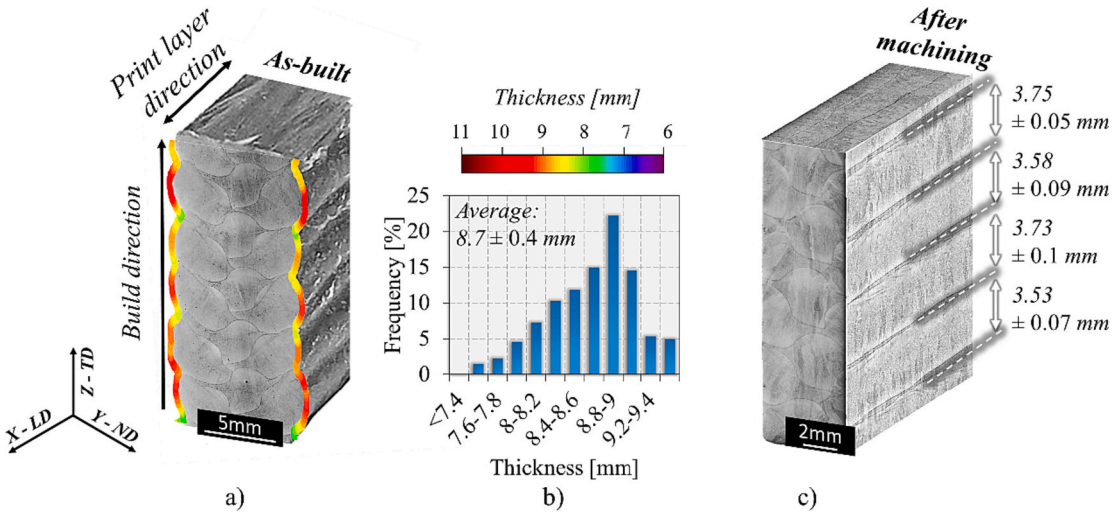

Fig. 7. Wall morphology for (a) the as-built condition, (b) histogram of the as-built wall thickness and (c) wall morphology for the machined condition.

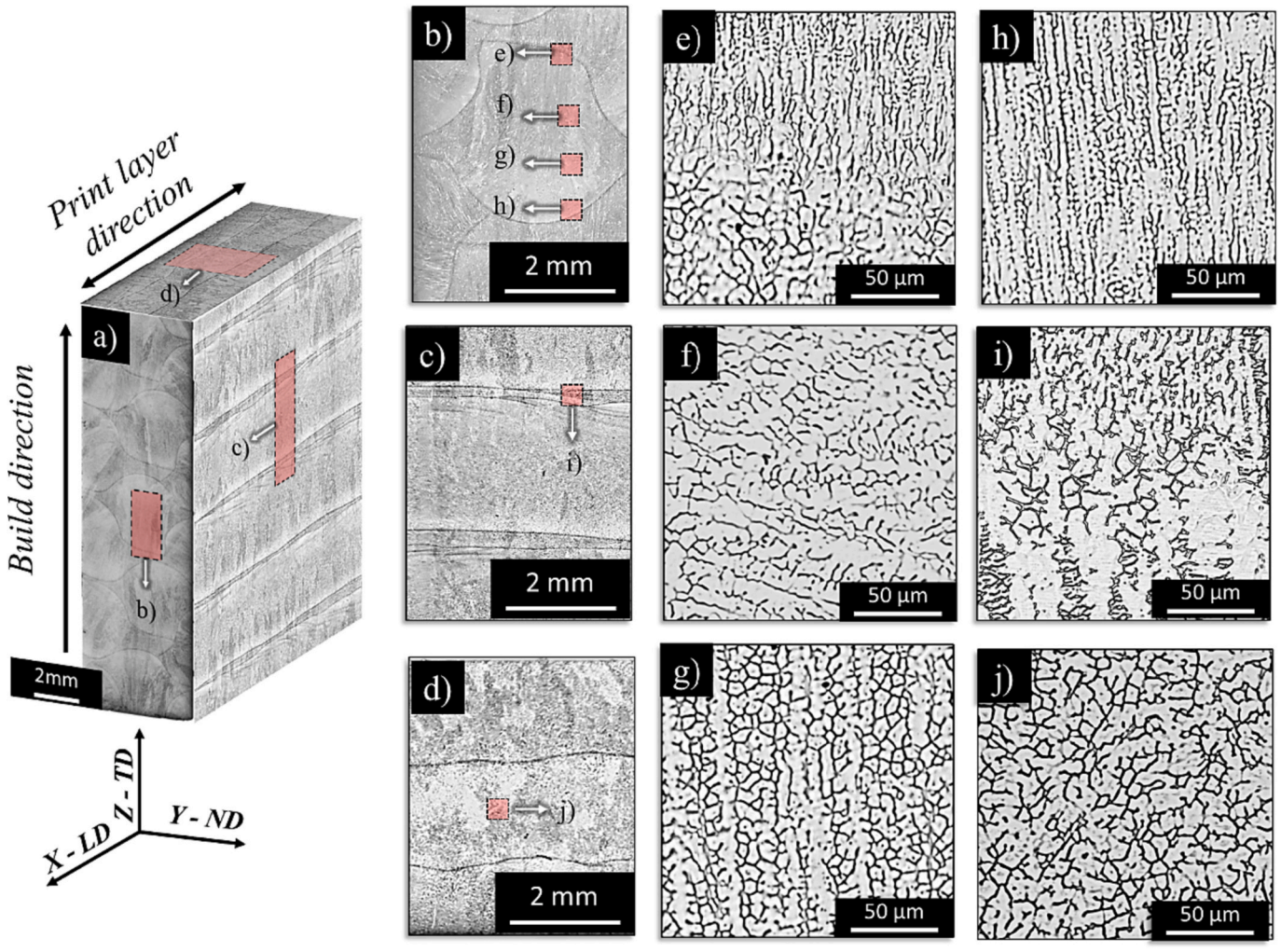

Fig. 8. Optical macrograph (a) and micrographs representing the microstructural evolution on the ND-TD (b, e to h), LD-TD (c and i) and LD-ND (d and j) planes.

direction. The periodic microstructural evolution observed in the ND-TD, LD-TD and LD-ND planes was kept constant all over the wall since, as already shown when analysing the thermal cycles, after layer six, the thermal history was similar independently of the wall region.

The solidification process can be better understood by calculating the SS alloy Cr equivalent (Cr_{eq}) and Ni equivalent (Ni_{eq}) values, using the following Eqs. [34]:

$$Cr_{eq} = \%Cr + \%Mo + 1.5\%Si + 0.5\%Nb, \quad (1)$$

$$Ni_{eq} = \%Ni + 30\%C + 0.5\%Mn. \quad (2)$$

According to Table 2, the Cr_{eq} and Ni_{eq} and the Cr_{eq}/Ni_{eq} ratio values for the feedstock wire are equal to 22.1%,12.6% and 1.75%, respectively, which according to the pseudobinary phase diagram of Fe–Cr–Ni [35], allows estimating that the main solidification mode is L → L+ δ → L + δ + γ → γ + δ, where L, γ and δ are the liquid, austenite and ferrite phases. During solidification, first the dendritic δ phase is formed. Afterwards, due to the non-equilibrium cooling conditions, some δ phase is preserved within the γ matrix, which leads to the formation of fine vermicular and lathy δ phases (black regions on the micrographs of Fig. 8) within the γ matrix (white regions on the micrographs of Fig. 8).

3.3. Assessment of the micro mismatch in mechanical properties

The presence of periodic microstructural bands along the building direction of the walls may be associated with some mismatch in mechanical properties, inside the printed layers, which may influence the walls macroscopic properties, namely, the isotropy in the mechanical properties. The homogeneity of the properties of the printed samples was assessed by performing hardness measurements. The harness profiles, in the ND-LD, TD-LD and ND-TD orientations, and the average hardness values, in each plane, calculated from the hardness profiles, are shown in Fig. 9a and b, respectively. The results show that the hardness measurements did not vary substantially in the different directions. Accordingly, the average hardness values, for the TD-LD, ND-LD and ND-TD were equal to 291 $HV_{0.2,}$ 251 $HV_{0.2}$ and 270 $HV_{0.2}$, which shows that no important mismatch in properties may be associated with the banded microstructure of the printed material.

3.4. Analysis of the mechanical properties of the as-built and machined walls

Fig. 10 shows the stress-strain curves obtained for the horizontal, vertical and inclined tensile specimens, in the as-built and machined conditions. For all samples, the fracture strain (ε_f), yield strength calculated at 0.2% proof stress (f_y) and ultimate tensile strength (f_u) were calculated as shown in Fig. 11. In addition, in Fig. 11, error bars indicating the maximum and minimum f_y, f_u and ε_f values registered for each type of tested condition, are also displayed.

Analysing the curves in Fig. 10, it is possible to conclude that all the tensile samples, regardless of their orientation and surface finishing, presented the typical nonlinear stress-strain behaviour, experiencing both elastic and plastic deformation prior to fracture.

Furthermore, Fig. 10 and Fig. 11, show that the mechanical properties of the tensile samples varied in accordance with the tested condition, where the yield stress was higher for the machined coupons. Fig. 11 shows that the machining of the walls increased 36%, 15% and 44% the average f_y values for the 0°, 45° and 90° samples, respectively. The results also show the effect of the coupon orientation on the yield stress, especially for the as-built coupons, where the vertical samples showed lower yield strength values. Depending on the orientation of the samples, a variation of 30% and 12% of the yield stress was observed for the as-built and machined samples, respectively. Comparing the error bars in Fig. 11, it is possible to observe a low scatter in the results registered for the machined samples, but some scatter in the f_y values for the as-built coupons. While for the machined coupons a deviation of around ±6 MPa, ± 13 MPa and ± 5 MPa on the f_y values was observed for the 0°, 45° and 90° samples, respectively, for the as-built samples a deviation of around ±33 MPa, ± 54 MPa and ± 3 MPa was reported.

The average f_u values, also shown in Fig. 11, display a similar evolution to that of the f_y, for the different tested conditions. This is, the machining operation leads to an increase of around 12%, 19% and 40% of the average f_u values for the 0°, 45° and 90° samples, respectively. Moreover, the as-built samples show an anisotropic behaviour. Varying the orientation of the samples from 0 to 90° resulted in a variation of 19% in the f_u values. On the contrary, the machined samples presented an isotropic behaviour since for the different orientations tested, only a difference of 6% in the f_u values was registered. The scatter bars for the machined samples show a tensile strength with reasonable reproducibility. A deviation of around ±20 MPa, ± 39 MPa and ± 24 MPa on the f_u values were observed for the as-built 0°, 45° and 90° samples, respectively, while for the machined coupons, a maximum and minimum deviation of around ±9 MPa, ± 8 MPa and ± 15 MPa were obtained.

In the same way, the machining of the coupons leads to an improvement of 15%, 34% and 133% of the average ε_f values for the 0°, 45° and 90° samples. For the as-built coupons, the ductility of the samples also varied in accordance with the principal axis of the tensile specimen, being maximum and minimum for the horizontal and vertical samples, respectively, i.e. varying the orientation of the samples from 0 to 90° resulted in a variation of 122% in the ε_f values. On the other hand, the machined coupons show a much lower anisotropic behaviour in terms of ductility, since varying the orientation of the principal axis of

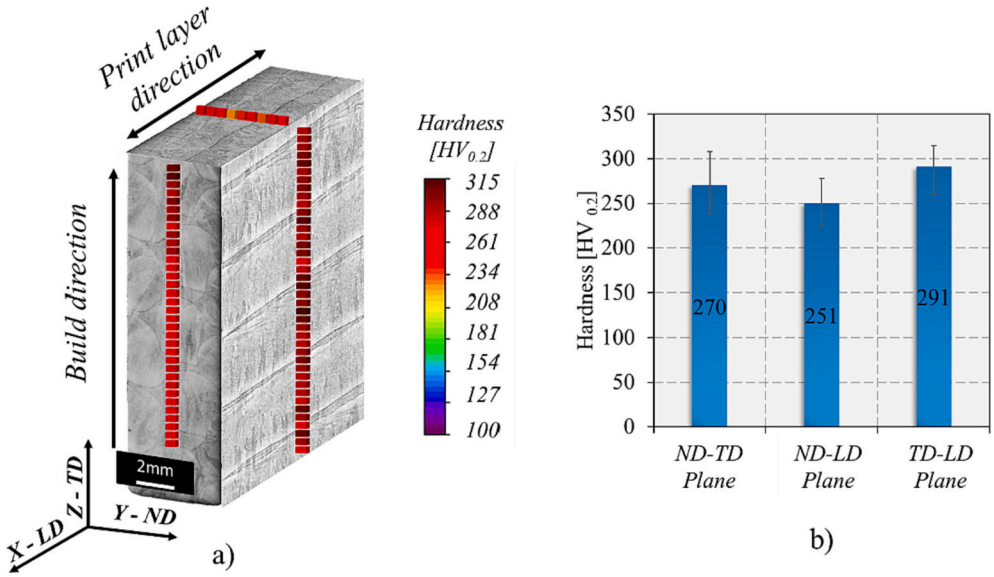

Fig. 9. (a) Hardness distribution map and (b) hardness average values along the TD-LD, ND-TD and ND-LD planes.

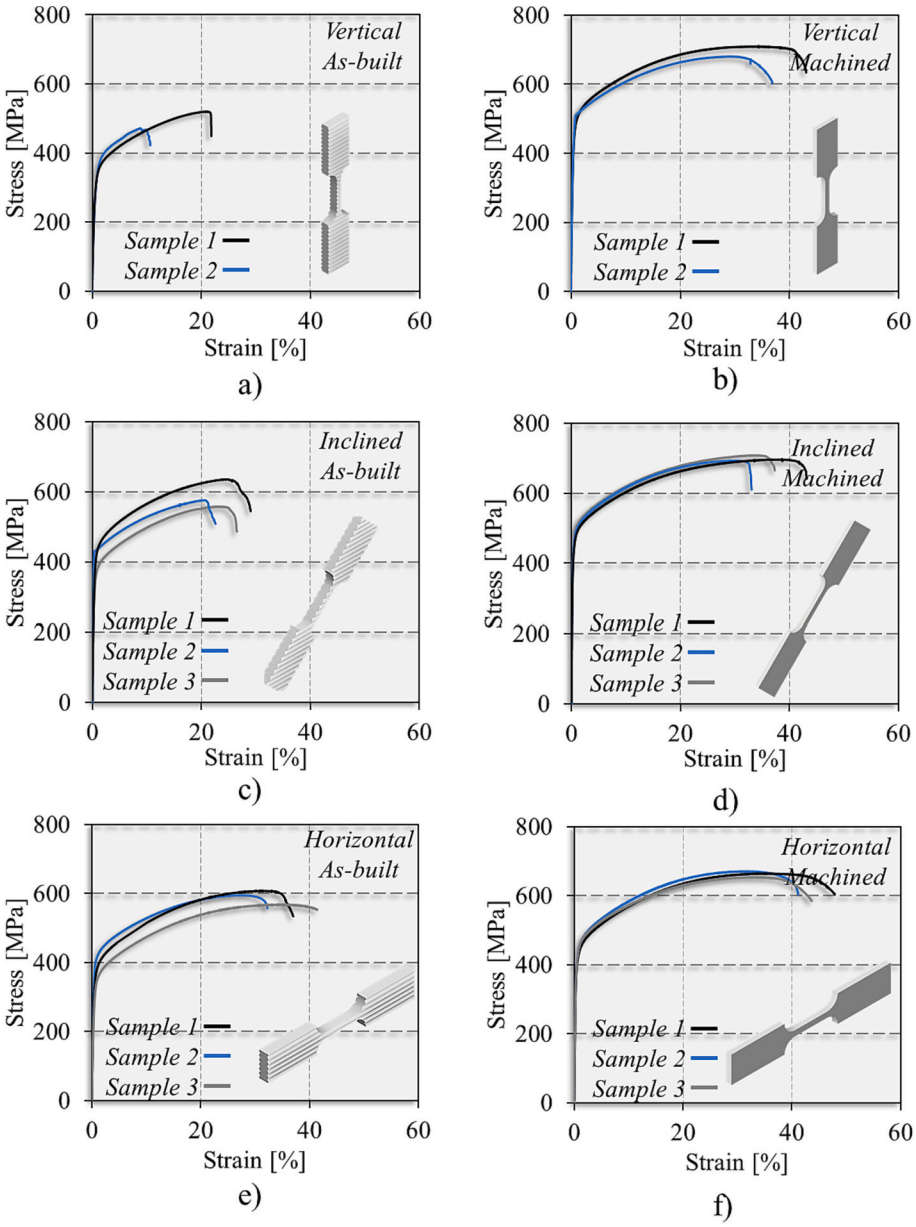

Fig. 10. Stress-strain curves for the (a and b) vertical (90°), (c and d) inclined (45°) and (e and f) horizontal (0°) coupons for the as-built and machined conditions.

the specimen only resulted in a variation of 18% in the ε_f values. Finally, analysing the error bars, the scatter of the ε_f results was almost identical for the machined and the as-built coupons. A deviation of around ±7%, ± 3% and ± 4% on the f_u values was observed for the as-built 0°, 45° and 90° samples, respectively, while for the machined coupons, a deviation of around ±4%, ± 5% and ± 3% was reported.

The analysis of the stress-strain curves shows that the f_y, f_u and ε_f values were always lower for the as-built coupons, due to the stress concentration originated by the periodically corrugated surface morphology that decreased the mechanical strength of the as-built samples. The WAAM surface morphology causes changes in the sample thickness and, consequently, variations in the tensile sample cross-section, that in turn, foster the scatter in the tensile properties.

The f_y, f_u and ε_f anisotropic response was always more evident for the as-built samples. Once again, this may be mainly attributed to the orientation of the corrugated surface morphology relative to the loading axis. In fact, the lower f_y, f_u and ε_f values observed for the vertical as-built samples resulted from the fact that for these coupons, the undulating direction is perpendicular to the loading axis, which results in a higher number of regions with varying thickness, i.e. consecutive zones with larger thickness followed by regions with reduced thickness (Fig. 7). Thus, removing the undulating surface promoted an increase in the f_y, f_u and ε_f isotropy for the machined samples.

Fig. 12 shows the high magnification views of the fracture surfaces in the central region for the vertical (Fig. 12a), horizontal (Fig. 12b) and inclined (Fig. 12c) orientations of the machined samples, and for the horizontal (Fig. 12d) orientation of the as-built sample. Regardless of the surface finishing or the printing orientation, it can be observed the main phenomenological features of ductile fracture. The figure also shows the presence of a reasonable uniform distribution of equiaxed dimples, which highlights the ductile mode of fracture. Furthermore, these large and homogeneously distributed dimples correlate well with high ductility values obtained for all tested conditions. The results are in agreement with the conclusions stated in previous studies [36–38]. Vora et al. 2022 [36] and Sasikumar et al. 2022 [37] studied the tensile properties of 316L stainless steel fabricated by GMAW-based WAAM and concluded that a large number of dimples with identical circulation on fracture surface indicates a good ductility. Jing et al. 2022 [38] reported

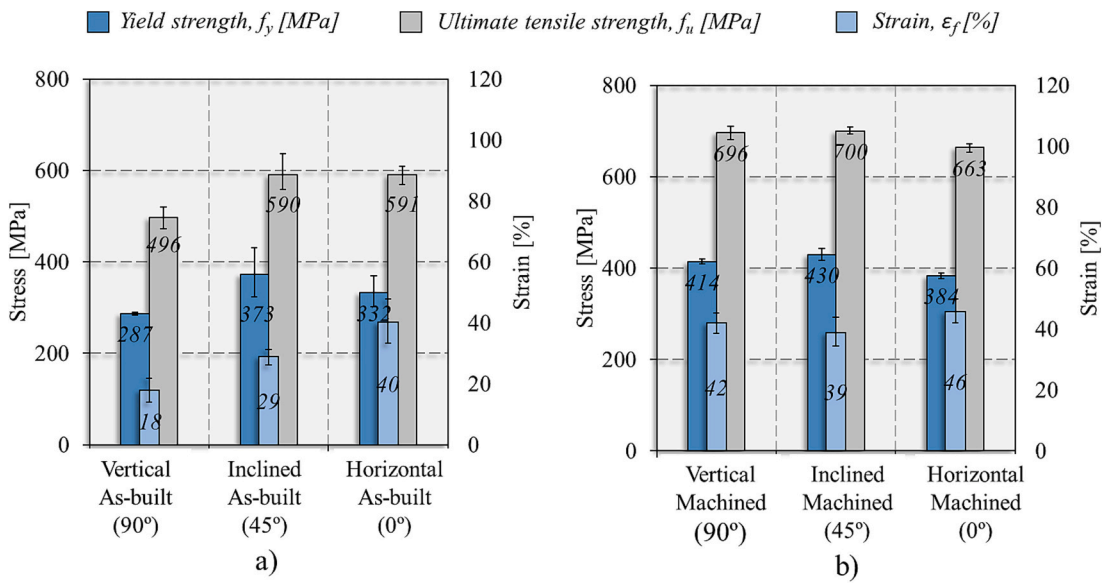

Fig. 11. Yield strength, ultimate tensile strength and failure strain values for the (a) as-built and (b) machined coupons with a relative angle of 0°, 45° and 90° between the building direction and the principal axis of the tensile specimen. The error bars indicate the maximum and minimum values registered.

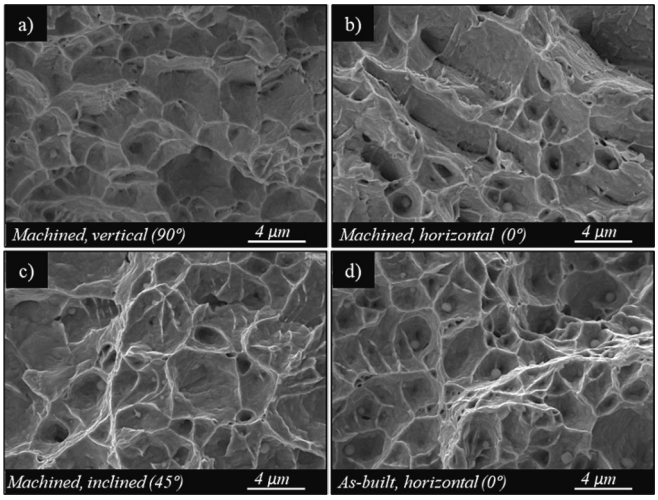

Fig. 12. High-magnification SEM micrograph of fracture surfaces for the vertical (a), horizontal (b) and inclined (c) machined samples and for the horizontal as-built sample (d).

the same outcomes for 304 L stainless steel manufactured via GTAW-based WAAM technology.

Fig. 13 and Fig. 14 compares the mechanical properties, i.e. the f_y, f_u and ε_f, respectively, obtained in the current work with the ones obtained by other works in 316L ASS WAAM parts [9,12,13,15,16,18,19,22,23,39] where different WAAM techniques, such as GMAW, GTAW and CMT, were used. In addition, the figures also provide information on tensile test surface finishing, i.e. if the sample was tested in the as-built or machined condition. The range of f_y and f_u obtained for the tensile samples with and without a machined surface are in the range of those obtained by the other authors. However, it is also important to verify if the WAAM SS satisfies the criteria established in the EN ISO 14343 standard [25], which are displayed in Fig. 13 and Fig. 14 by the red lines, where the minimum f_y, f_u and ε_f values should be superior to 320 MPa, 510 MPa and 25%, respectively (Table 3). While the machined coupons meet the requirements established by the standard for all cases, the as-built coupons, in general, do not meet the same requirement. Although the maximum and average f_y, f_u and ε_f values fulfil the standard requirements, the minimum f_y, f_u and ε_f values are lower than those defined for this SS.

3.5. Material modelling

Although various analytical models may be used to describe stress-strain curves, verifying their suitability to describe the mechanical properties of components produced by additive manufacturing processes is necessary, since accurately describing the curve roundedness, strain hardening and strain at the ultimate tensile strength is essential for the design of structures. The nonlinear stress-strain curves exhibited in Fig. 10 may be represented by the two-stage Ramberg-Osgood modified model proposed by Mirambell and Real [40]:

$$\varepsilon = \begin{cases} \dfrac{\sigma}{E} + 0.002\left(\dfrac{\sigma}{f_y}\right)^n & for\ \sigma \le f_y \\ \dfrac{\sigma - f_y}{E_{0.2}} + \left(\varepsilon_u - \varepsilon_{0.2} - \dfrac{f_u - f_y}{E_{0.2}}\right)\left(\dfrac{\sigma - f_y}{f_u - f_y}\right)^m & for\ f_y < \sigma \le f_u \end{cases} \quad (3)$$

where E is the material Young's modulus, $E_{0.2}$ is the tangent modulus of the stress-strain curve at the 0.2% proof stress, given by

$$E_{0.2} = \frac{E}{1 + 0.002n\frac{E}{f_y}} \quad (4)$$

$\varepsilon_{0.2}$ is the total strain at the 0.2% proof stress, defined by

$$\varepsilon_{0.2} = 0.002 + \frac{f_y}{E}, \quad (5)$$

and n and m are the strain hardening coefficients, which according to EN 1993-1-4 [41], may be calculated by

$$n = \frac{ln(20)}{ln\left(\frac{f_y}{\sigma_{0.01}}\right)} \quad (6)$$

$$m = 1 + 3.5\frac{f_y}{\sigma_u} \quad (7)$$

where $\sigma_{0.01}$ represents the 0.01% proof stress. The ε_u is the strain at the material ultimate tensile strength f_u and may be calculated by

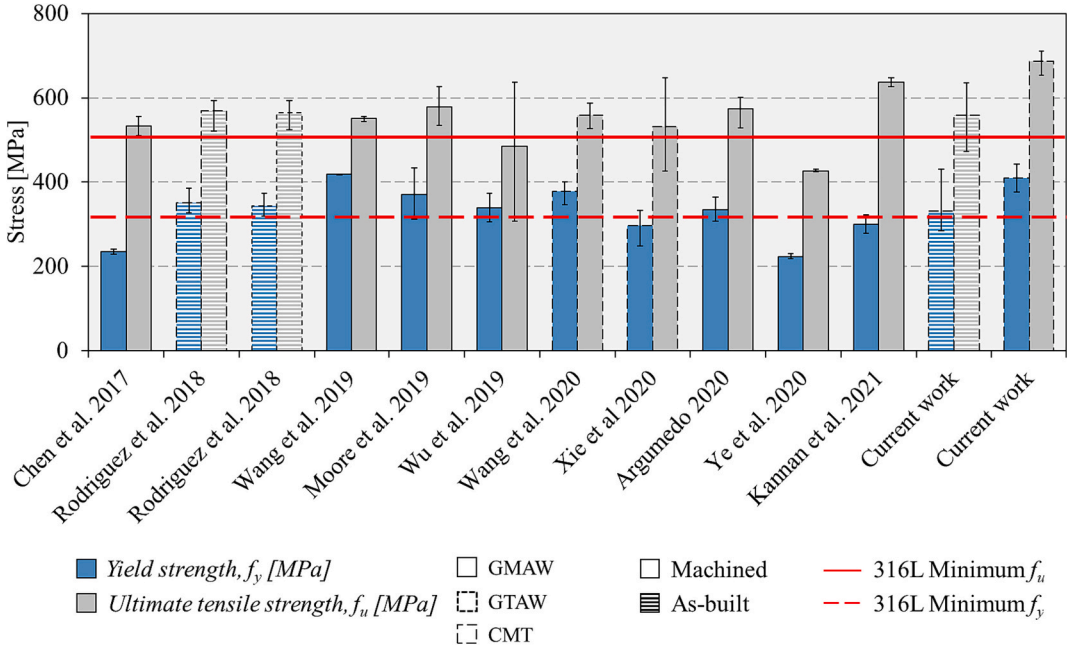

Fig. 13. Range of f_y, and f_u values obtained for WAAM 316L austenitic SS parts produced by other authors.

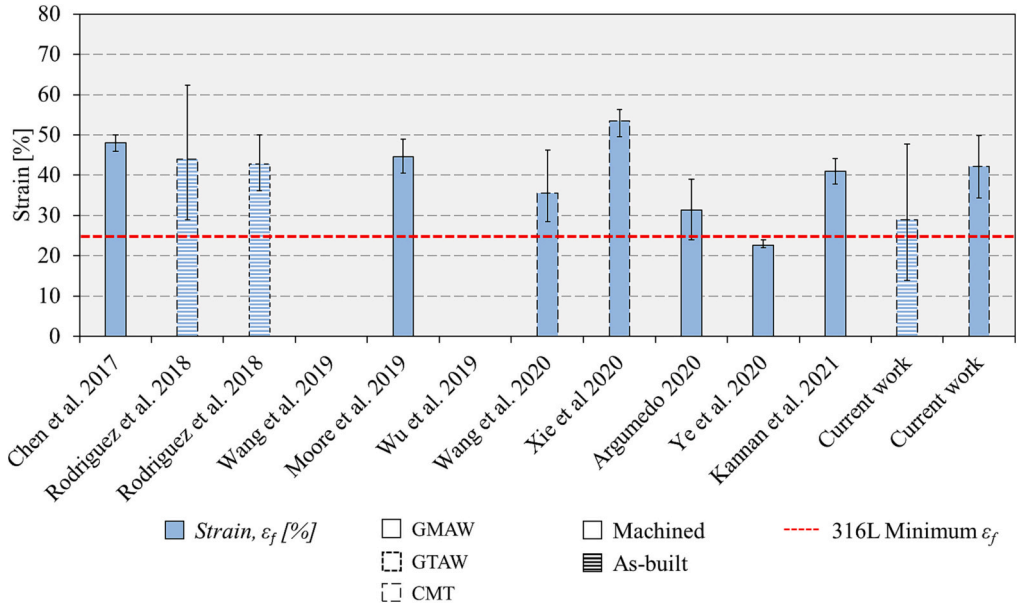

Fig. 14. Range of ε_f values obtained for WAAM 316L austenitic SS parts produced by other authors.

$$\varepsilon_u = C_3\left(1-\frac{f_y}{f_u}\right)+C_4, \tag{8}$$

where C_3 and C_4 are constants. According to EN 1993-1-4 [41] and Gardner et al. 2023 [42], for stainless steels, and C_3 and C_4 constants may be equal to 1 and 0, respectively.

Fig. 15 plots the ε_u values against the 1-f_y/f_u ratio, together with the predictive expression given in Eq. 8. In the figure, the data from current work, represented by black circles, are compared with experimental data from the literature, where the white circles correspond to the values obtained for ASS produced by conventional manufacturing techniques [43] and the blue circles correspond to values obtained from parts produced by WAAM in the 308LSi ASS [44]. In addition, in Fig. 15a and b, the WAAM data correspond to tensile coupons tested in the machined and as-built conditions, respectively. The comparison reveals that the ε_u values for the WAAM machined coupons are in agreement with the predictive expression used for the conventional ASS. On the contrary, the same trend is not verified for the ε_u values of the WAAM coupons in the as-built condition, where the curve slope is inferior due to the material corrugated surface morphology which results in lower ductility. Therefore, updated coefficients to predict the ε_u values were determined, using the least squares optimisation method, for the as-built samples. The revised equation is shown in Fig. 15b, where the C_3 and C_4 constants are equal to 0.6 and 0, respectively. Table 4 shows the statistical results where the experimental values for the strain at the material ultimate tensile strength, $\varepsilon_{u,exp}$, were normalized by the predicted material ultimate tensile strength, $\varepsilon_{u,model}$, calculated in accordance with the EN 1993-1-4 and through the proposed coefficients.

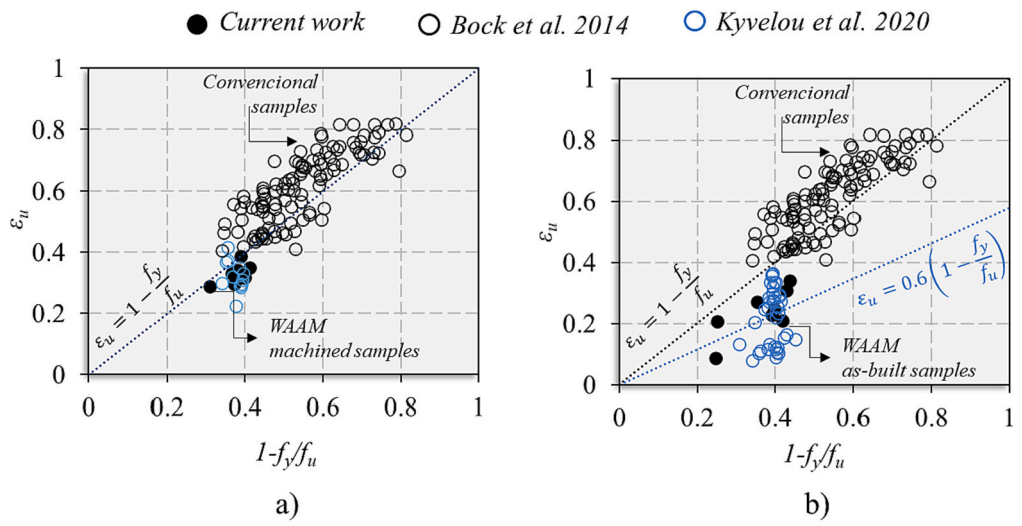

Fig. 15. – Comparison between the evolution of the ε_u values with the $1\text{-}f_y/f_u$ ratio for different austenitic stainless steels produced by conventional manufacturing techniques (white circles) and by WAAM process (black and blue circles) in the (a) machined and (b) as-built condition. (For interpretation of the references to colour in this figure legend, the reader is referred to the web version of this article.)

According to Table 4, for the as-built WAAM components, it is demonstrated that the revised coefficients delivers satisfactory average predictions for the $\varepsilon_{u,exp}$ data, accompanied by a moderate coefficient of variation.

The accuracy of Eq. 6 to calculate the first strain hardening exponent n can be assessed in Fig. 16 which compares the evolution of the n_{model} predicted values, through Eq. 6 (blue points), with those obtained experimentally, n_{exp}, through the least squares optimisation method for the as-built (square points) and machined samples (circle points). In the figure, an alternative equation, see Eq. (9), proposed by other authors [40,45,46] is also represented by a black dashed line, which imposes that the analytical curve passes through the 0.05% and the 0.2% proof stresses.

$$n = \frac{ln(4)}{ln\left(\frac{f_y}{\sigma_{0.05}}\right)} \tag{9}$$

The correlation coefficients, shown in Fig. 16, allow to conclude that Eq. 9 provides considerably more accurate predictions for n values than those obtained with Eq. 6. In Table 5 is shown the comparison of the n values for ASS, produced by conventional manufacturing techniques, with the average n values of ASS produced by WAAM for the as-built and machined conditions. According to the table, the n values obtained for the WAAM parts are closer to the ones obtained for conventional ASS produced by hot rolling process than by cold forming, which present a sharper yielding curve.

Finally, in Fig. 17, the graphics show the evolution of the second strain hardening exponent m against the f_y/σ_u ratio, together with the predictive expression given by Eq. 7 (black dashed line). The data from

Table 4
Statistical outcomes for the $\varepsilon_{u,exp}/\varepsilon_{u,model}$ results for different models.

	Austenitic stainless steels			
Model	$\varepsilon_{u,exp}/\varepsilon_{u,model}$ EN 1993-1-4 ($C_3 = 1$; $C_4 = 0$)	$\varepsilon_{u,exp}/\varepsilon_{u,model}$ EN 1993-1-4 ($C_3 = 1$; $C_4 = 0$)	$\varepsilon_{u,exp}/\varepsilon_{u,model}$ EN 1993-1-4 ($C_3 = 1$; $C_4 = 0$)	$\varepsilon_{u,exp}/\varepsilon_{u,model}$ Proposed coefficients ($C_3 = 0.6$; $C_4 = 0$)
Manufacturing process	Conventional	WAAM: machined	WAAM: as-built	WAAM: as-built
Mean	1.04	0.87	0.58	0.96
Coefficient of variation	0.28	0.14	0.22	0.35

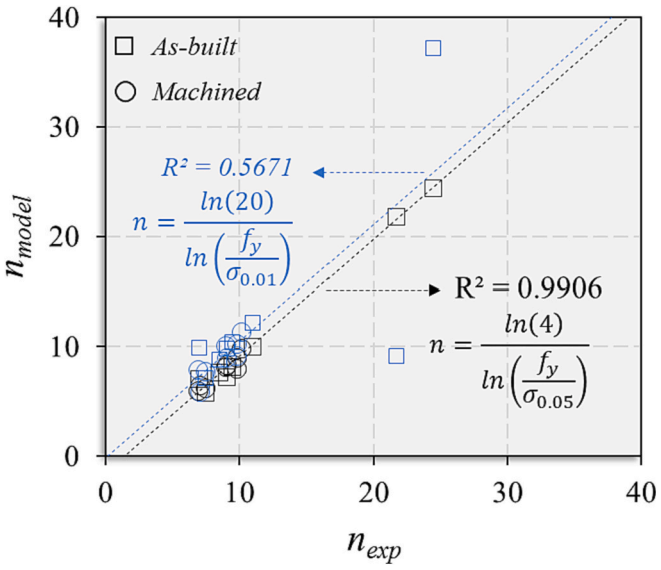

Fig. 16. Comparison between the predicted (n_{model}) and experimental (n_{exp}) strain hardening values.

Table 5
Comparison of the strain hardening exponents n for austenitic stainless steels produced by conventional manufacturing techniques and by and by WAAM process for the as-built and machined conditions.

Source	Grade	Product Type	n
Arrayago et al. 2015 [46]	1.4301	Sheet	10.2
		Sheet	11.8
		Cold-Formed	7.9
		Cold-Formed	4.8
	1.4435	Sheet	11.8
	1.4541	Sheet	10.7
	1.4307	Sheet	11.8
	1.4571	Cold-formed	6.8
	1.4404	Cold-formed	7.2
	1.4318	Cold-formed	5.2
Kyvelou et al. 2020 [44]	308LSi feedstock wire	WAAM Machined	12.0
		WAAM as-built	11.8
Current work	316LSi feedstock wire	WAAM Machined	8.7
		WAAM as-built	12.3

the current work, represented by black circles, for the machined (Fig. 17a) and as-built conditions (Fig. 17b) was compared with experimental data from the literature, where the white circles correspond to the values obtain for ASS produced by conventional manufacturing techniques [46], and the blue circles correspond to values obtained from parts produced by WAAM using 308LSi ASS [44]. Furthermore, in the figure, the curve given by Eq. 7 is compared with an alternative equation (blue dashed line), proposed by Arrayago et al. 2015 [46], to predict the m values, which can be written as follows

$$m = 1 + 2.8\frac{f_y}{\sigma_u}. \tag{10}$$

Analysing the figure, it is possible to conclude that the m values obtained for the WAAM parts follow a similar trend to the m values determined for ASS produced with conventional techniques. Table 6 shows the statistical analysis where the strain hardening values obtained experimentally m_{exp}, through the least squares optimisation method were normalized by the predicted values m_{model} calculated according to Eq. 7 and Eq. 10. According to the table, the model proposed by Arrayago et al. 2015 [43] provided an improved prediction for the m values, since independently of the manufacturing process or surface condition, the mean $m_{exp/}\ m_{model}$ ratios were always lower when Eq. 10 was used, while the coefficient of variation was identical for both models.

4. Conclusions

This paper analysed the tensile and microstructural properties of 316LSi walls produced by CMT-WAAM. The key findings are:

- During deposition, the temperature gradients were higher in the building than in the printing direction. For the first layers, the substrate has an important role in the heat dissipation however, with the increase of the layer height, the thermal history became constant, reaching steady state conditions. A constant interlayer temperature of around 700 °C was reached for the processing parameters and deposition strategy tested.
- The wall microstructure presented a regular semi-elliptical morphology along the building direction, with vermicular and lathy δ phases within the γ matrix.
- The machined coupons always exhibited better mechanical properties than the as-built ones. The machining operation led to an average increase of around 32%, 24% and 61% in the yield strength, ultimate tensile strength and failure strength, respectively. Furthermore, while the machined samples presented isotropic mechanical properties, the as-built samples presented anisotropy due to their rough surface finish.
- The fracture surfaces of the as-built and the machined samples, irrespective of the printing orientation, exhibited a ductile failure mode. The SEM images also enable to confirm that no defects, such as micro pores or micro inclusions, were present in the deposited material.
- Since no major defects, such as cracks, pores or improper fusion zones, were present in the produced samples, the tensile properties of the wall, for the machined condition, satisfied the criteria established for industrial applications.
- The material models available in the literature were found to accurately represent the uniaxial stress-strain behaviour of austenitic stainless steel manufactured by WAAM. The elastic and plastic strain hardening behaviour for the additive manufacturing parts was similar to that observed for materials manufactured by conventional methods. The only difference was observed for the strain values at the material ultimate tensile strength of WAAM components tested in the as-built condition. However, to extrapolate and develop more generic models it is still imperative to conduct additional research encompassing a wider range of processing parameters, material compositions, and manufacturing strategies.

Finally, despite the current study provides valuable insights concerning the understanding of WAAM of stainless steel parts, it is evident that there remains an extensive scope for future research in this field. Future investigations should envisage a comprehensive global analysis, incorporating a wider range of processing parameters and experimental setups. With this data, it will be possible to establish an extensive database correlating WAAM parameters and procedures with the mechanical properties of the produced parts, the microstructural features, the morphology, the dimensional accuracy, the residual stresses, and the formation of defects such as warpage, delamination, and internal voids, among others. This holistic approach is essential for the ongoing advancement and optimisation of WAAM processes across various applications.

CRediT authorship contribution statement

D.G. Andrade: Formal analysis, Investigation, Validation, Writing – original draft. **T. Tankova:** Conceptualization, Funding acquisition, Investigation, Methodology, Writing – review & editing. **C. Zhu:** Investigation, Methodology, Writing – review & editing. **R. Branco:**

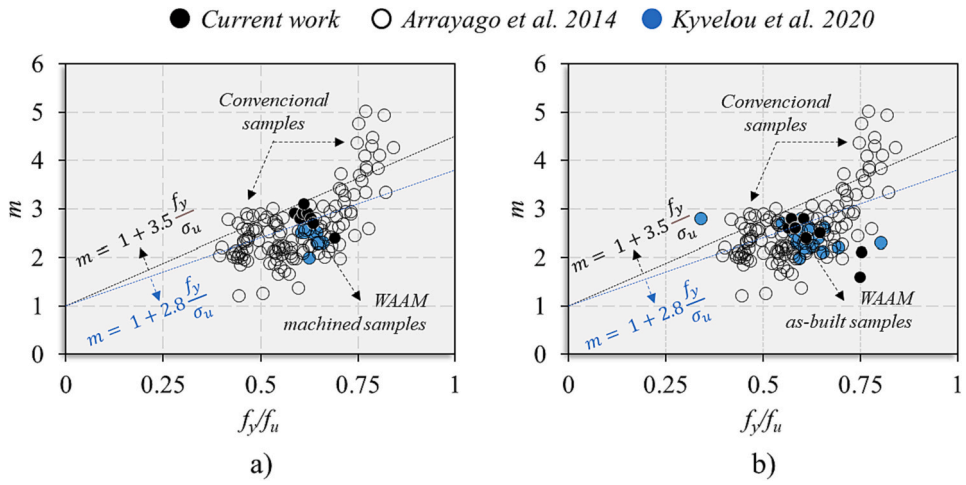

Fig. 17. Comparison between the evolution of the m values with the f_y/f_u ratio for different austenitic stainless steels produced by conventional manufacturing techniques (white circles) and by WAAM process (black and blue circles) in the (a) machined and (b) as-built conditions. (For interpretation of the references to colour in this figure legend, the reader is referred to the web version of this article.)

Table 6
Statistical outcomes for the m_{exp}/m_{model} results calculated with different models.

Austenitic stainless steels						
Model	$\varepsilon_{u,exp}/\varepsilon_{u,model}$ EN 1993-1-4 (Eq. 7)			$\varepsilon_{u,exp}/\varepsilon_{u,model}$ Arrayago et al. 2015 (Eq. 10)		
Manufacturing process	Conventional	WAAM: machined	WAAM: as-built	Conventional	WAAM: machined	WAAM: as-built
Mean	0.84	0.82	0.77	0.97	0.95	0.89
Coefficient of variation	0.20	0.12	0.15	0.20	0.12	0.15

Investigation, Writing – review & editing. **L. Simões da Silva:** Conceptualization, Supervision, Validation, Writing – review & editing. **D.M. Rodrigues:** Conceptualization, Methodology, Supervision, Validation, Writing – review & editing.

Declaration of competing interest

The authors declare that they have no known competing financial interests or personal relationships that could have appeared to influence the work reported in this paper.

Data availability

Data will be made available on request.

Acknowledgements

This research is sponsored by FCT/MCTES through national funds (PIDDAC) under the R&D Unit Institute for Sustainability and Innovation in Structural Engineering (ISISE), under reference UIDB/04029/2020 (doi.org/10.54499/UIDB/04029/2020); under the Associate Laboratory Advanced Production and Intelligent Systems ARISE under reference LA/P/0112/2020, under the Centre for Mechanical Engineering, Materials and Processes (CEMMPRE), under reference UIDB/00285/2020; and by the AMCONSTRUCTION project, which is part of the UC PATRONAGE 2019 initiative and a joint effort between CEMMPRE and ISISE. The author, C. Zhu is supported by the Portuguese Foundation for Science and Technology through the grant with reference 2021.05992.BD. All supports are gratefully acknowledged.

References

[1] T.A. Rodrigues, V. Duarte, R.M. Miranda, T.G. Santos, J.P. Oliveira, Current status and perspectives on wire and arc additive manufacturing (WAAM), Materials (Basel) 12 (2019), https://doi.org/10.3390/ma12071121.
[2] K. Treutler, V. Wesling, The current state of research of wire arc additive manufacturing (Waam): a review, Appl. Sci. 11 (2021), https://doi.org/10.3390/app11188619.
[3] J. Müller, M. Grabowski, C. Müller, J. Hensel, J. Unglaub, K. Thiele, H. Kloft, K. Dilger, Design and parameter identification of wire and arc additively manufactured (WAAM) steel bars for use in construction, Metals (Basel) 9 (2019), https://doi.org/10.3390/met9070725.
[4] L. Gardner, P. Kyvelou, G. Herbert, C. Buchanan, Testing and initial verification of the world's first metal 3D printed bridge, J. Constr. Steel Res. 172 (2020), https://doi.org/10.1016/j.jcsr.2020.106233.
[5] C. Greer, A. Nycz, M. Noakes, B. Richardson, B. Post, T. Kurfess, L. Love, Introduction to the design rules for metal big area additive manufacturing, Addit. Manuf. 27 (2019) 159–166, https://doi.org/10.1016/j.addma.2019.02.016.
[6] G. Ma, G. Zhao, Z. Li, M. Yang, W. Xiao, Optimization strategies for robotic additive and subtractive manufacturing of large and high thin-walled aluminum structures, Int. J. Adv. Manuf. Technol. 101 (2019) 1275–1292, https://doi.org/10.1007/s00170-018-3009-3.
[7] Stainless Steel in Figures, World Stainl. Assoc, 2022. https://www.worldstainless.org/files/issf/non-image-files/PDF/Stainless_Steel_in_Figures_2022_public_English.pdf (accessed October 13, 2022).
[8] J. Long, M. Wang, W. Zhao, X. Zhang, Y. Wei, W. Ou, High-power wire arc additive manufacturing of stainless steel with active heat management, Sci. Technol. Weld. Join. 27 (2022) 256–264, https://doi.org/10.1080/13621718.2022.2045127.
[9] X. Chen, J. Li, X. Cheng, B. He, H. Wang, Z. Huang, Microstructure and mechanical properties of the austenitic stainless steel 316L fabricated by gas metal arc additive manufacturing, Mater. Sci. Eng. A 703 (2017) 567–577, https://doi.org/10.1016/j.msea.2017.05.024.
[10] J. Park, S.H. Lee, Cmt-based wire arc additive manufacturing using 316l stainless steel (2): solidification map of the multilayer deposit, Metals (Basel) 11 (2021), https://doi.org/10.3390/met11111725.
[11] S.H. Lee, CMT-based wire arc additive manufacturing using 316l stainless steel: effect of heat accumulation on the multi-layer deposits, Metals (Basel) 10 (2020), https://doi.org/10.3390/met10020278.
[12] L. Wang, J. Xue, Q. Wang, Correlation between arc mode, microstructure, and mechanical properties during wire arc additive manufacturing of 316L stainless steel, Mater. Sci. Eng. A 751 (2019) 183–190, https://doi.org/10.1016/j.msea.2019.02.078.
[13] C. Wang, T.G. Liu, P. Zhu, Y.H. Lu, T. Shoji, Study on microstructure and tensile properties of 316L stainless steel fabricated by CMT wire and arc additive manufacturing, Mater. Sci. Eng. A 796 (2020), https://doi.org/10.1016/j.msea.2020.140006.
[14] J. Wanwan, Z. Chaoqun, J. Shuoya, T. Yingtao, W. Daniel, L. Wen, Wire arc additive manufacturing of stainless steels: a review, Appl. Sci. 10 (2020) 1563.
[15] A.R. Kannan, S.M. Kumar, R. Pramod, N.S. Shanmugam, M. Vishnukumar, S. Naveenkumar, Microstructural characterization and mechanical integrity of stainless steel 316L clad layers deposited via wire arc additive manufacturing for nuclear applications, Mater. Werkst. 52 (2021) 617–623, https://doi.org/10.1002/mawe.202000242.
[16] B. Xie, J. Xue, X. Ren, Wire arc deposition additive manufacturing and experimental study of 316l stainless steel by cmt + p process, Metals (Basel) 10 (2020) 1–19, https://doi.org/10.3390/met10111419.
[17] B.S.I. Welding, BS EN 1011-1:2009. Welding — Recommendations for welding of metallic materials. Part 1: General guidance for arc welding, 2001.
[18] N. Rodriguez, L. Vázquez, I. Huarte, E. Arruti, I. Tabernero, P. Alvarez, Wire and arc additive manufacturing: a comparison between CMT and TopTIG processes applied to stainless steel, Weld. World 62 (2018) 1083–1096, https://doi.org/10.1007/s40194-018-0606-6.
[19] W. Wu, J. Xue, L. Wang, Z. Zhang, Y. Hu, C. Dong, S.A. Manufacturing, Forming process, microstructure, and mechanical properties of thin-walled 316L stainless steel using speed-cold-welding additive manufacturing, Metals (Basel) 9 (2019), https://doi.org/10.3390/met9010109.
[20] J. Chen, H. Wei, X. Zhang, Y. Peng, J. Kong, K. Wang, Flow behavior and microstructure evolution during dynamic deformation of 316 L stainless steel fabricated by wire and arc additive manufacturing, Mater. Des. 198 (2021) 109325, https://doi.org/10.1016/j.matdes.2020.109325.
[21] L. Belotti, J.A.W. van Dommelen, M.G.D. Geers, C. Goulas, W. Ya, J.P. M. Hoefnagels, Microstructural characterisation of thick-walled wire arc additively manufactured stainless steel, J. Mater. Process. Technol. 299 (2022), https://doi.org/10.1016/j.jmatprotec.2021.117373.
[22] C. Ye, G. Lu, X. Peng, S. Hou, J. Zhou, L. Ni, Microstructure and mechanical properties of the 316 stainless steel nuclear grade experimental component made by wire and arc additive manufacturing, Proc. Inst. Mech. Eng. Part C J. Mech. Eng. Sci. 234 (2020) 4258–4267, https://doi.org/10.1177/0954406220920692.
[23] P. Moore, A. Addison, M. Nowak-Coventry, Mechanical properties of wire plus arc additive manufactured steel and stainless steel structures, Weld. World 63 (2019) 1521–1530, https://doi.org/10.1007/s40194-019-00775-4.
[24] D. Yang, G. Wang, G. Zhang, Thermal analysis for single-pass multi-layer GMAW based additive manufacturing using infrared thermography, J. Mater. Process. Technol. 244 (2017) 215–224, https://doi.org/10.1016/j.jmatprotec.2017.01.024.
[25] ISO-14343, Welding consumables - Wire electrodes, strip electrodes, wires and rods for arc welding of stainless and heat resisting steels - Classification, 2017.
[26] Y. Balram, T. Vishu Vardhan, B. Sridhar Babu, G. Venkat Ramana, C. Preethi, Thermal stress analysis of AISI 316 stainless steels weldments in TIG and pulse TIG welding processes, Mater. Today Proc. 19 (2019) 182–187, https://doi.org/10.1016/j.matpr.2019.06.695.
[27] Y. Balram, G. Rajyalakshmi, Thermal fields and residual stresses analysis in TIG weldments of SS 316 and Monel 400 by numerical simulation and experimentation, Mater. Res. Express 6 (2019) 0865e2, https://doi.org/10.1088/2053-1591/ab23cf.
[28] A.E. Patterson, S.L. Messimer, P.A. Farrington, C.L. Carmen, J.T. Kendrick, Experimental design approach for studying overhanging features in selective laser melting, J. Adv. Manuf. Technol. 13 (2019) 15–32. https://jamt.utem.edu.my/jamt/article/view/5502.
[29] M.H. Farshidianfar, A. Khajepour, A.P. Gerlich, Effect of real-time cooling rate on microstructure in laser additive Manufacturing, J. Mater. Process. Technol. 231 (2016) 468–478, https://doi.org/10.1016/j.jmatprotec.2016.01.017.
[30] A. Ashby, G. Guss, R.K. Ganeriwala, A.A. Martin, P.J. DePond, D.J. Deane, M. J. Matthews, C.L. Druzgalski, Thermal history and high-speed optical imaging of overhang structures during laser powder bed fusion: a computational and experimental analysis, Addit. Manuf. 53 (2022) 102669, https://doi.org/10.1016/j.addma.2022.102669.

[31] ISO-6892-1, Metallic materials – Tensile testing – Part 1: Method of test at room temperature, 2019.
[32] ISO/TR 20580:2022, Preparation of metallographic specimens, 2022.
[33] Y. Huang, M. Ansari, H. Asgari, M.H. Farshidianfar, D. Sarker, M.B. Khamesee, E. Toyserkani, Rapid prediction of real-time thermal characteristics, solidification parameters and microstructure in laser directed energy deposition (powder-fed additive manufacturing), J. Mater. Process. Technol. 274 (2019) 116286, https://doi.org/10.1016/j.jmatprotec.2019.116286.
[34] A.L. Schaeffler, Constitution diagram for stainless steel weld metal, Met. Prog. 56 (1949) 680.
[35] J.C. Lippold, W.F. Savage, Solidification of austenitic stainless steel weldments: part 2—the effect of alloy composition on ferrite morphology, Weld. J. (Miami, Fla) 59 (1980).
[36] J. Vora, H. Parmar, R. Chaudhari, S. Khanna, M. Doshi, V. Patel, Experimental investigations on mechanical properties of multi-layered structure fabricated by GMAW-based WAAM of SS316L, J. Mater. Res. Technol. 20 (2022) 2748–2757, https://doi.org/10.1016/j.jmrt.2022.08.074.
[37] R. Sasikumar, A.R. Kannan, S.M. Kumar, R. Pramod, N.P. Kumar, N.S. Shanmugam, Y. Palguna, S. Sivankalai, 316L and IN625 : Microstructural and mechanical perspectives, CIRP J. Manuf. Sci. Technol. 38 (2022) 230–242, https://doi.org/10.1016/j.cirpj.2022.05.005.
[38] C. Jing, Z. Chen, B. Liu, T. Xu, J. Wang, T. Lu, J. Lu, Y. Guo, C. Liu, Materials Science & Engineering a Improving mechanical strength and isotropy for wire-arc additive manufactured 304L stainless steels via controlling arc heat input, Mater. Sci. Eng. A 845 (2022) 143223, https://doi.org/10.1016/j.msea.2022.143223.
[39] J. Galan Argumedo, Fatigue Behavior and Mechanical Characterization of Austenitic Stainless-Steel Components Produced through Wire+ Arc Additive Manufacturing, 2020.
[40] E. Mirambell, E. Real, On the calculation of deflections in structural stainless steel beams: an experimental and numerical investigation, J. Constr. Steel Res. 54 (2000) 109–133, https://doi.org/10.1016/S0143-974X(99)00051-6.
[41] EN1993-1-4, Eurocode 3: design of steel structures – part 1-4: general rules – supplementary rules for stainless steels, Brussels Eur. Comm. Stand, 2006.
[42] L. Gardner, X. Yun, F. Walport, The continuous strength method – review and outlook, Eng. Struct. 275 (2023), https://doi.org/10.1016/j.engstruct.2022.114924.
[43] M. Bock, L. Gardner, E. Real, Material and local buckling response of ferritic stainless steel sections, Thin-Walled Struct. 89 (2015) 131–141, https://doi.org/10.1016/j.tws.2014.12.012.
[44] P. Kyvelou, H. Slack, D. Daskalaki Mountanou, M.A. Wadee, T. Ben Britton, C. Buchanan, L. Gardner, Mechanical and microstructural testing of wire and arc additively manufactured sheet material, Mater. Des. 192 (2020) 108675, https://doi.org/10.1016/j.matdes.2020.108675.
[45] E. Real, I. Arrayago, E. Mirambell, R. Westeel, Comparative study of analytical expressions for the modelling of stainless steel behaviour, Thin-Walled Struct. 83 (2014) 2–11, https://doi.org/10.1016/j.tws.2014.01.026.
[46] I. Arrayago, E. Real, L. Gardner, Description of stress-strain curves for stainless steel alloys, Mater. Des. 87 (2015) 540–552, https://doi.org/10.1016/j.matdes.2015.08.001.